Journal of Power Sources 196 (2011) 8019–8030

Contents lists available at ScienceDirect

Journal of Power Sources

journal homepage: www.elsevier.com/locate/jpowsour

Multiple concentric spirals for the flow field of a proton exchange membrane fuel cell

Daniel Juarez-Robles, Abel Hernandez-Guerrero*, Bladimir Ramos-Alvarado, Francisco Elizalde-Blancas, Cesar E. Damian-Ascencio

Department of Mechanical Engineering, University of Guanajuato, Mexico

ARTICLE INFO

Article history:
Received 22 March 2011
Received in revised form 6 May 2011
Accepted 12 May 2011
Available online 19 May 2011

Keywords:
Three-dimensional
Non-isothermal
Single phase
PEM fuel cell
Entropy generation
Numerical

ABSTRACT

The present analysis considers a three-dimensional non-isothermal model in a single phase of a PEM fuel cell with a flow field path in the shape of 1, 2, 3, 4, 6, and 8 concentric spirals. The current density contours, the water content and the entropy generated in all zones of the fuel cell are predicted. The analysis of the three-dimensional model includes the gas flow channels in the six geometric shapes mentioned above, the current collectors, gas diffusion layers, catalyst layers on both sides of the model, anode and cathode, and a proton exchange membrane in between. The energy equation, mass conservation, and transport of species equations are solved, including source terms that take into account the electrochemical effects occurring inside the cell. Also, the entropy generation equation is added to the governing equations of the model. The results allow a comparison to help to decide which of the 6 analyzed configurations improve the performance of the fuel cell, increasing the current density produced, reducing the pressure drop and producing the most uniform current density. The entropy generation analysis reveals the effects that cause the most significant losses (irreversibilities) in the cell. The Bejan number and the Π number are used to compare the irreversibilities produced by the matter flow and by the heat transfer for each one of the six models.

1. Introduction

Fuel cells are electrochemical devices that convert the chemical energy of a fuel directly to electrical energy. There is a whole family of fuel cells that can be characterized by the electrolyte used. All of these fuel cells function in the same basic way. At the anode, a fuel (usually hydrogen) is dissociated, while at the cathode oxygen is reduced to oxide species.

The proton exchange membrane fuel cell, PEMFC, derives its name from the special membrane used as the electrolyte. The electrochemical reactions that take place inside the cell are:

$$H_2 \rightarrow 2H^+ + 2e^- \quad (1)$$

$$\tfrac{1}{2}O_2 + 2H^+ + 2e^- \rightarrow H_2O \quad (2)$$

Proton exchange membrane fuel cells have gained a lot of popularity amongst scientists due to their operating conditions, high density of energy generated and the portable capabilities of these devices.

Fig. 1 shows the cross section of a PEM fuel cell. The main components of a PEMFC are the current collectors, the gas diffusion layers (GDL's), the catalysts layers and the proton exchange membrane. The main factors that determine the fuel cell performance are the operating conditions, the reactant's humidity, the properties of the materials and the flow distribution of the gases in the MEA by means of the geometry of the gas channels.

The geometries of the bipolar plates have been the object of many studies. The serpentine shape [1,2] has proved to have a good performance as a flow distributor, with the inconvenient of producing larger pressure drops caused mainly by the numerous sudden, sharp turns. The parallel channels geometry [3] is a bad gas distributor causing larger concentration gradients. The geometry called interdigitated [4,5] is also a deficient gas distributor because it produces flooding zones (although its performance improves when the operating pressure increases.) These 3 geometries are already considered as conventional due to their wide commercial use.

Recently, new and non-conventional flow configurations for the flow field of the PEMFC have been reported in the technical literature. These results reveal the fact that the fuel cells require a multi objective optimization to make them an option to replace fossil fuel based technologies. The main objective behind those designs is to improve the fuel cell performance, developing larger current densities in smaller areas. These designs, such as the radial [6,7], the constructal theory-based [8,9], the biomimetical [10], the tree net-

* Corresponding author. Tel.: +52 464 6479940x2382; fax: +524646479940x2311.
E-mail address: abelh@salamanca.ugto.mx (A. Hernandez-Guerrero).

0378-7753/$ – see front matter © 2011 Elsevier B.V. All rights reserved.
doi:10.1016/j.jpowsour.2011.05.029

Nomenclature

A	Area (cm^2)
a_k	Water activity on stream k
Be	Bejan number
D_i	Diffusivity of the i species ($m^2\ s^{-1}$)
F	Faraday constant (96,487 C mol^{-1})
h_{react}	Heat of water formation ($W\ m^{-3}$)
I	Current density ($A\ m^{-2}$)
j_i	Diffusion mass flux of the i species ($kg\ m^{-2}\ s^{-1}$)
j_k^{ref}	Reference current density on stream k ($A\ m^{-3}$)
M_i	Molecular weight of the i species ($kg\ kmol^{-1}$)
n	Number of turns
n_d	Electrosmotic drag coefficient
P	Total pressure (Pa)
Q	Volumetric flow rate ($m^3\ s^{-1}$)
$\bar{q}$	Heat rate (W)
R	Universal gas constant (8.314 kJ $kmol^{-1}\ K^{-1}$)
R_k	Exchange current density ($A\ m^{-3}$)
R_{ohm}	Ohmic resistance ($\Omega\ m$)
T	Temperature (K)
V	Velocity ($m\ s^{-1}$)
V_{oc}	Open circuit voltage (V)
V_{cell}	Cell voltage (V)
W_{elec}	Electric power density ($W\ cm^{-2}$)
X_i	Molar fraction of the i species
Y_i	Mass fraction of the i species

Greek symbols

α	Transfer coefficient
β	Permeability (m^2)
ε	Porosity
ϕ_k	Potential field in the k interface (V)
γ	Concentration coefficient
η	Overpotential (V)
λ	Water content
μ	Dynamic viscosity ($kg\ s\ m^{-2}$)
Π	Pi number
ρ	Density ($kg\ m^{-3}$)
σ	Electric conductivity ($\Omega^{-1}\ m^{-1}$)
σ^s	Entropy generation ($W\ K^{-1}$)
ζ	Stoichiometric flow rate

B. Subscripts/superscripts

a	Anode
act	Activation
c	Cathode
cat	Catalyst
i	H_2, O_2, H_2O
HT	Heat
H_2	Hydrogen
H_2O	Water
k	Anode or cathode
MD	Mechanical dissipation
MEA	Membrane electrode assembly
MF	Matter flow
mem	Membrane
O_2	Oxygen
ref	Reference
sat	Saturation
sol	Solid
w	Water
wv	Water vapor

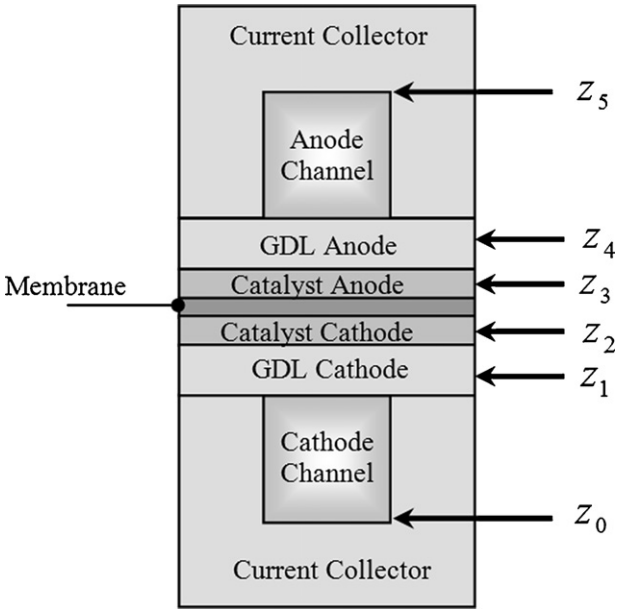

Fig. 1. Cross section of the fuel cell. Regions where the source terms are defined.

work [11,12], the spiral [13,14], and the fractal [15] are named after the geometric shape or the theory used to build them. Although these new designs present improvements they still have deficiencies in comparison with the conventional ones. Amongst these deficiencies are the poor active area utilization which leads to low current density production; and high ohmic losses due to a deficient contact area between the current collectors and the electrode. These deficiencies are inherent to the structural design.

All real processes present irreversibilities that can be associated to friction, mass transfer, heat transfer, electrochemical reactions, etc., resulting in a non desirable loss or degradation of energy quality. This loss of efficiency is related to the entropy generation. The generation of entropy is a synonym for the potential destruction of system energy; its minimization has been used as the optimal design criteria for thermal systems. The mechanisms of entropy generation must be understood [16,17] by analyzing the process itself and its thermal, hydrodynamic and geometric characteristics in order to obtain an optimal configuration with a minimum loss of available energy. Damian et al. [18] presented the entropy generation analysis of a PEMFC with a biomimetical flow field. Their analysis consists of not only the calculation of the total entropy generated, but also an analysis of the impact of the entropy generation on each of the different processes involved on the cell performance. Their results indicate that the flow and thermal effects are smaller than the entropy generated by the transport of species.

The present work shows the results for the overall performance and entropy generation of a PEMFC with multiple spirals as flow fields. The results of the entropy analysis are compared with the performance analysis to have a complete description of the cell performance in the hope of finding the most efficient geometric shape.

2. Model development

The present work is a numerical analysis of six fuel cells with $n = 1$, 2, 3, 4, 6 and 8 flow channels of constant width, see Fig. 2. The geometries are generated using concentric Archimedes' spirals, $r = a\theta$, with a $2\pi/n$ radian phase angle between each couple of spirals. This allows generating two channels of constant width.

A computational three-dimensional model is built for each of the 6 geometries considered. The models are used to analyze the

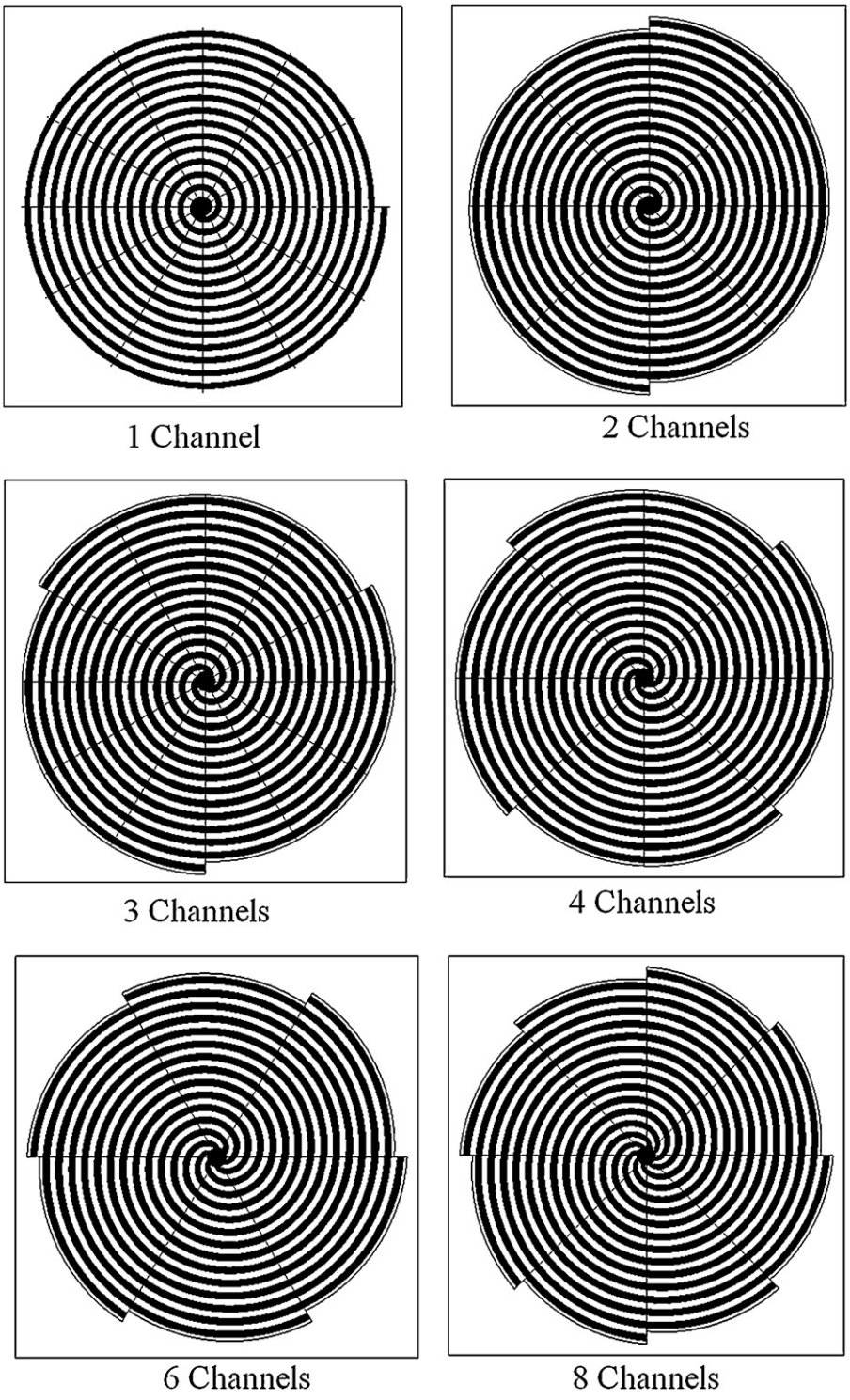

Fig. 2. Geometry of the fuel cells analyzed.

electrochemical reactions and the transport phenomena occurring at the catalyst layers (at both the anode and the cathode side). In other areas, such as the gas diffusion layer, no chemical reactions occur.

The geometric dimensions are listed in Table 1. These dimensions are similar to the dimensions used by Shimpalee and Dutta [1]. The current collectors, GDL, catalysts layers, and the membrane have the same width as the cell.

The gas flow channels and the current collectors are the zones of the cell that are adapted to the new geometry, see Fig. 2. The rest of the fuel cell zones: GDL's, catalyst layers, anode and cathode, and also the membrane, are not affected by this geometry change. The number of turns varies in such a way that the reaction area is the same for all the models.

Fig. 3 shows the three-dimensional model developed for the 8 channel fuel cell, where the gas reactant inlets are located at the center of the spirals. The outlets are located on the outer part of the spirals. It is important to note that the gas entrance is not at the same level as the cell. A straight circular conduct is added to consider the acrylic base upon which the fuel cell is mounted. The fuel

Table 1
Model dimensions.

Description	Dimension
Current collector height	1.50×10^{-3} m
Channels height	1.00×10^{-3} m
Channels width	0.80×10^{-3} m
GDL height	0.50×10^{-3} m
Catalyst width	0.03×10^{-3} m
Cell width	1.60×10^{-3} m
Inlet radius	0.53×10^{-3} m
Inlet channel length	3.50×10^{-3} m
Number of turns (1-channel)	13.75
Number of turns (2-channels)	6.375
Number of turns (3-channels)	4.666
Number of turns (4-channels)	3.187
Number of turns (6-channels)	2.333
Number of turns (8-channels)	1.718
Reaction area	16.6×10^{-4} m^2

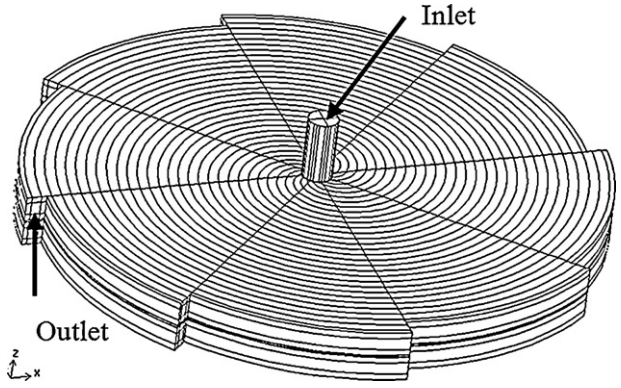

Fig. 3. Boundary conditions for the 3-dimensional model of the 8-channel fuel cell.

cell cross section area defined previously in Fig. 1 can be appreciated as the spiral branches out.

3. Model assumptions

Steady state, laminar flow, non-isothermal, single phase, isotropic materials, and mass transport along three dimensions are assumed in the analysis. The open circuit voltage at the cell temperature is $V_{oc} = 1.0904$ V.

4. Governing equations

The governing equations including the source terms are listed in Table 2. The added source terms due to the electrochemical effects are listed in Table 3. The 'z' indicators in Fig. 1 show the zones where the source terms are calculated.

The mass diffusion flux, $J_{i,l}$, in the species transport equation is defined as

$$J_{i,l} = -\rho D_l \frac{\partial m_l}{\partial x_i} \tag{17}$$

where D_i [19] is defined as,

$$D_i = \varepsilon^{1.5} D_i^0 \left(\frac{p_0}{p}\right) \left(\frac{T}{T_0}\right)^{1.5} \tag{18}$$

Here $p_0 = 101325$ N m^{-2} and $T_0 = 300$ K. D_i already considers the porosity effects. The electrosmotic drag coefficient is calculated using the following equation,

$$\alpha_d = \frac{2.5\lambda}{22} \tag{19}$$

while the water diffusion coefficient at the membrane, D_w, is that proposed by Nguyen and White [20], i.e.

$$D_w = 5.5 \times 10^{-11} \alpha_d \exp\left[2416\left(\frac{1}{303} - \frac{1}{T_S}\right)\right] \tag{20}$$

Table 3
Source terms.

Source terms and location of application (see Fig. 1)

$$S_m = S_{H_2} + S_{aw} \quad at\ z = z_3 \qquad S_m = S_{O_2} + S_{cw} \quad at\ z = z_2 \tag{10}$$

$$\left.\begin{aligned} S_{px} &= -\frac{\mu u}{\beta_x} \\ S_{py} &= -\frac{\mu v}{\beta_y} \\ S_{pz} &= -\frac{\mu w}{\beta_z} \end{aligned}\right\} \quad \text{at } z_1 \le z \le z_4 \tag{11}$$

$$S_h = I^2 R_{ohm} + h_{react} + \eta_{act} R_{a;c} \quad \text{at all zones} \tag{12}$$

$$S_{H_2} = -\frac{M_{H_2}}{2F} R_a \quad \text{at } z = z_3 \tag{13}$$

$$S_{aw} = -\frac{M_{H_2O}}{F} R_a \quad \text{at } z = z_3 \tag{14}$$

$$S_{O_2} = -\frac{M_{O_2}}{4F} R_c \quad \text{at } z = z_2 \tag{15}$$

$$S_{cw} = \frac{M_{H_2O}}{2F} R_c \quad \text{at } z = z_2 \tag{16}$$

Table 2
Governing equations.

Governing equations	Mathematical expressions	
Continuity	$\frac{\partial(\rho u)}{\partial x} + \frac{\partial(\rho v)}{\partial y} + \frac{\partial(\rho w)}{\partial z} = S_m$	(3)
Momentum transport	$u\frac{\partial(\rho u)}{\partial x} + v\frac{\partial(\rho u)}{\partial y} + w\frac{\partial(\rho u)}{\partial z} = -\frac{\partial P}{\partial x} + \frac{\partial}{\partial x}\left(\mu\frac{\partial u}{\partial x}\right) + \frac{\partial}{\partial y}\left(\mu\frac{\partial u}{\partial y}\right) + \frac{\partial}{\partial z}\left(\mu\frac{\partial u}{\partial z}\right) + S_{px}$ $u\frac{\partial(\rho v)}{\partial x} + v\frac{\partial(\rho v)}{\partial y} + w\frac{\partial(\rho v)}{\partial z} = -\frac{\partial P}{\partial y} + \frac{\partial}{\partial x}\left(\mu\frac{\partial v}{\partial x}\right) + \frac{\partial}{\partial y}\left(\mu\frac{\partial v}{\partial y}\right) + \frac{\partial}{\partial z}\left(\mu\frac{\partial v}{\partial z}\right) + S_{py}$ $u\frac{\partial(\rho w)}{\partial x} + v\frac{\partial(\rho w)}{\partial y} + w\frac{\partial(\rho w)}{\partial z} = -\frac{\partial P}{\partial z} + \frac{\partial}{\partial x}\left(\mu\frac{\partial w}{\partial x}\right) + \frac{\partial}{\partial y}\left(\mu\frac{\partial w}{\partial y}\right) + \frac{\partial}{\partial z}\left(\mu\frac{\partial w}{\partial z}\right) + S_{pz}$	(4)
Energy	$u\frac{\partial(\rho CT)}{\partial x} + v\frac{\partial(\rho CT)}{\partial y} + w\frac{\partial(\rho CT)}{\partial z} = \frac{\partial}{\partial x}\left(k\frac{\partial T}{\partial x}\right) + \frac{\partial}{\partial y}\left(k\frac{\partial T}{\partial y}\right) + \frac{\partial}{\partial z}\left(k\frac{\partial T}{\partial z}\right) + S_h$	(5)
Hydrogen transport (anode side)	$u\frac{\partial\left(\rho m_{H_2}\right)}{\partial x} + v\frac{\partial\left(\rho m_{H_2}\right)}{\partial y} + w\frac{\partial\left(\rho m_{H_2}\right)}{\partial z} = \frac{\partial\left(J_{x,H_2}\right)}{\partial x} + \frac{\partial\left(J_{y,H_2}\right)}{\partial y} + \frac{\partial\left(J_{z,H_2}\right)}{\partial z} + S_{H_2}$	(6)
Water transport (Anode side)	$u\frac{\partial(\rho m_{aw})}{\partial x} + v\frac{\partial(\rho m_{aw})}{\partial y} + w\frac{\partial(\rho m_{aw})}{\partial z} = \frac{\partial(J_{x,aw})}{\partial x} + \frac{\partial(J_{y,aw})}{\partial y} + \frac{\partial(J_{z,aw})}{\partial z} + S_{aw}$	(7)
Oxygen transport cathode side)	$u\frac{\partial\left(\rho m_{O_2}\right)}{\partial x} + v\frac{\partial\left(\rho m_{O_2}\right)}{\partial y} + w\frac{\partial\left(\rho m_{O_2}\right)}{\partial z} = \frac{\partial\left(J_{x,O_2}\right)}{\partial x} + \frac{\partial\left(J_{y,O_2}\right)}{\partial y} + \frac{\partial\left(J_{z,O_2}\right)}{\partial z} + S_{O_2}$	(8)
Water transport (cathode side)	$u\frac{\partial(\rho m_{cw})}{\partial x} + v\frac{\partial(\rho m_{cw})}{\partial y} + w\frac{\partial(\rho m_{cw})}{\partial z} = \frac{\partial(J_{x,cw})}{\partial x} + \frac{\partial(J_{y,cw})}{\partial y} + \frac{\partial(J_{z,cw})}{\partial z} + S_{cw}$	(9)

The saturation pressure is calculated with the correlation proposed by Springer [21], in atm, as,

$$\log_{10}P_{\mathrm{Sat}} = -2.1794 + 0.02953\,(T - 273.17) - 9.1837 \times 10^{-5}(T - 273.17)^2 + 1.4454 \times 10^{-7}(T - 273.17)^3 \quad (21)$$

The membrane phase electric conductivity, σ_{mem}, is calculated using the equation also proposed by Springer [21], namely,

$$\sigma_{\mathrm{mem}} = \varepsilon\,(0.514\lambda - 0.326)\exp\left[1268\left(\frac{1}{303} - \frac{1}{T}\right)\right] \quad (22)$$

while the water content is calculated with the correlation used by Springer [21],

$$\lambda = \begin{cases} 0.043 + 17.18a_{\mathrm{a}} - 39.85a_{\mathrm{a}}^2 + 36.0a_{\mathrm{a}}^3 & a_{\mathrm{a}} \le 1 \\ 14.0 + 1.4\,(a_{\mathrm{a}} - 1) & a_{\mathrm{a}} > 1 \end{cases} \quad (23)$$

here a_{a} is the water activity defined as

$$a_{\mathrm{a}} = \frac{P_{\mathrm{wv}}}{P_{\mathrm{sat}}} \quad (24)$$

Two potential equations are solved in the model; one potential equation accounts for the electron transport through the solid materials and the other represents the protonic transport of H^+. The potential equations are defined as

$$\nabla\,(\sigma_{\mathrm{sol}}\nabla\phi_{\mathrm{sol}}) + R_{\mathrm{sol}} = 0 \quad (25)$$

$$\nabla\,(\sigma_{\mathrm{mem}}\nabla\phi_{\mathrm{mem}}) + R_{\mathrm{mem}} = 0 \quad (26)$$

The transfer current or source terms are nonzero only inside the catalyst layers and are determined as $R_{\mathrm{sol}} = -R_{\mathrm{a}}$ for the solid phase at the anode side and $R_{\mathrm{sol}} = +R_{\mathrm{c}}$ at the cathode side. For the membrane phase, $R_{\mathrm{mem}} = +R_{\mathrm{a}}$ at the anode side and $R_{\mathrm{mem}} = -R_{\mathrm{c}}$ at the cathode side.

The source terms in Eqs. (26) and (27) are calculated via the Butler–Vollmer equation, namely,

$$R_{\mathrm{a}} = j_{\mathrm{a}}^{\mathrm{ref}}\left(\frac{[H_2]}{[H_2]_{\mathrm{ref}}}\right)^{\gamma_{\mathrm{a}}}\left[\exp\left(\frac{\alpha_{\mathrm{a}}F\eta_{\mathrm{a}}}{\mathrm{RT}}\right) - \exp\left(\frac{\alpha_{\mathrm{c}}F\eta_{\mathrm{a}}}{-\mathrm{RT}}\right)\right] \quad (27)$$

$$R_{\mathrm{c}} = j_{\mathrm{c}}^{\mathrm{ref}}\left(\frac{[\mathrm{O}_2]}{[\mathrm{O}_2]_{\mathrm{ref}}}\right)^{\gamma_{\mathrm{c}}}\left[\exp\left(\frac{\alpha_{\mathrm{c}}F\eta_{\mathrm{c}}}{-\mathrm{RT}}\right) - \exp\left(\frac{\alpha_{\mathrm{a}}F\eta_{\mathrm{c}}}{\mathrm{RT}}\right)\right] \quad (28)$$

The overpotentials at the anode and cathode sides are found from

$$\eta_{\mathrm{a}} = \phi_{\mathrm{sol}} - \phi_{\mathrm{mem}} \quad (29)$$

$$\eta_{\mathrm{c}} = \phi_{\mathrm{sol}} - \phi_{\mathrm{mem}} - V_{\mathrm{oc}} \quad (30)$$

while the open circuit reference voltage [22] is given by

$$V_{\mathrm{oc}} = 0.0025T + 0.2329 \quad (31)$$

where T represents the operation cell temperature.

The total entropy generation is calculated as follows [23]:

$$\sigma^{\mathrm{s}} = \bar{q}\nabla\left(\frac{1}{T}\right) - \sum_{k=1}^{N} J_k\nabla\left(\frac{\mu_k}{T}\right) - \frac{1}{T}p^{\mathrm{v}}\nabla u - \overset{\mathrm{o}}{P}{}^{\mathrm{u}} : \nabla u \quad (32)$$

From Eq. (32) it is clear that three different effects contribute to the rate of entropy production, namely: the entropy production related to heat transfer, the second term to the matter flow and the third and fourth to mechanical dissipation. Thus, the entropy production can be expressed as:

$$\sigma^{\mathrm{s}} = \sigma_{\mathrm{HT}}^{\mathrm{s}} + \sigma_{\mathrm{MF}}^{\mathrm{s}} + \sigma_{\mathrm{MD}}^{\mathrm{s}} \quad (33)$$

The total entropy production is obtained through integration of the local entropy generation (σ) in each computational domain:

$$\sigma_{\mathrm{T,i}}^{\mathrm{s}} = \int_V \sigma_{\mathrm{i}}^{s}\,dV \quad (34)$$

An alternative parameter to represent the distribution of irreversibilities is the Bejan number (Be) defined as [17]:

$$\mathrm{Be} = \frac{\sigma_{\mathrm{HT}}^{\mathrm{s}}}{\sigma^{\mathrm{s}}} \quad (35)$$

When the entropy generation is due only to mechanical dissipation and heat transfer, this dimensionless number indicates that heat transfer irreversibilities are dominant when $\mathrm{Be} \gg 1/2$. However, in fuel cells the entropy generation depends mainly on the matter diffusion. For this reason, the parameter proposed by Damian et al. [18] is used:

$$\Pi = \frac{\sigma_{\mathrm{MF}}^{\mathrm{s}}}{\sigma^{\mathrm{s}}} \quad (36)$$

This parameter is the ratio of entropy generation due to the matter flow to the total entropy. This number implies that irreversibilities due to matter flow are insignificant when $\Pi \ll 1/3$.

5. Boundary conditions

The boundary conditions assumed for the computational domain are shown in Fig. 4. At the inlet of the gas flow channels, the boundary condition is given by the stoichiometric flow rate:

$$\zeta_{\mathrm{a}} = X_{\mathrm{H_2,in}}Q_{\mathrm{a,in}}\frac{P_{\mathrm{a}}}{RT}\frac{2F}{I_{\mathrm{ref}}A_{\mathrm{MEA}}} \quad (38)$$

$$\zeta_{\mathrm{c}} = X_{\mathrm{O_2,in}}Q_{\mathrm{c,in}}\frac{P_{\mathrm{c}}}{RT}\frac{4F}{I_{\mathrm{ref}}A_{\mathrm{MEA}}} \quad (39)$$

A zero-gauge pressure condition is defined at the outlets to simulate a discharge to the atmosphere. The external faces of the current collectors are defined as a *wall* with the condition of a potentiostatic cell, i.e. the electric potential at the anode is $\phi_{\mathrm{sol}} = 0$ and at the cathode $\phi_{\mathrm{sol}} = V_{\mathrm{cell}}$.

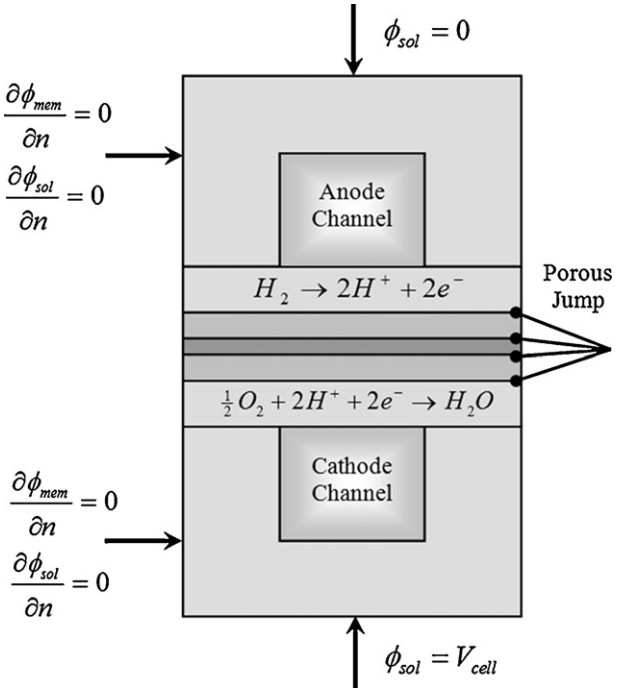

Fig. 4. Boundary conditions at the fuel cell.

Table 4
Operating conditions.

Parameter	Value
Pressure	202650 Pa
Cell temperature	343 K
Humidity at the anode side	100%
Humidity at the cathode side	100%
Anode stoichiometric flow rate	1.5
Cathode stoichiometric flow rate	2

Table 5
Electrochemical parameters.

Property	Value
Current collector conductivity [25]	$\sigma_{sol} = 1.25 \times 10^5\ \Omega^{-1}\ m^{-1}$
GDL and catalyst conductivity [25]	$\sigma_{cat} = \sigma_{GDL} = 53\ \Omega^{-1}\ m^{-1}$
GDL porosity [24]	$\varepsilon_{GDL} = 0.4$
Catalyst porosity [24]	$\varepsilon_{cat} = 0.112$
Concentration exp. (anode) [24]	$\gamma_a = 0.5$
Concentration exp. (cathode) [24]	$\gamma_c = 1$
Transfer coefficient (anode) [24]	$\alpha_a = 2$
Transfer coefficient (cathode) [24]	$\alpha_c = 2$
Ref. current density (anode) [24]	$j_a^{ref} = 1 \times 10^9\ A\ m^{-3}$
Ref. current density (cathode) [24]	$j_c^{ref} = 3 \times 10^5\ A\ m^{-3}$
Hydrogen reference diffusivity [24]	$D^0_{H_2} = 1.1 \times 10^{-4}\ m^2\ s^{-1}$
Oxygen reference diffusivity [24]	$D^0_{O_2} = 3.2 \times 10^{-5}\ m^2\ s^{-1}$
Water reference diffusivity [24]	$D^0_{H_2O} = 7.35 \times 10^{-5}\ m^2\ s^{-1}$
Nitrogen reference diffusivity [12]	$D^0_{N_2} = 8 \times 10^{-5}\ m^2\ s^{-1}$
Permeability [12]	$\beta = 2 \times 10^{-10}\ m^2$

The terminal walls are defined as adiabatic, while the side walls are defined at the cell temperature.

6. Operating conditions

The model was analyzed under the operating conditions listed in Table 4.

The electrochemical parameters employed in the numerical model are listed in Table 5.

7. Numerical procedure

The mesh quality was verified and refined in order to avoid having a model with highly skewed elements. Fig. 5 shows the mesh quality distribution for the 8-channel model, the one with the larger number of highly skewed elements.

A mesh-independence analysis was conducted varying the total number of elements. The grid-independence was verified via the continuity equation's solution. The final mesh for the 6 models had an average of 1 million elements.

A finite volume code is used to solve the coupled equations of mass conservation, mass diffusion and momentum conservation. The code includes a module that takes into account the electrochemical effects of the source terms associated with each zone. The numerical procedure is as follows: the Navier–Stokes equations are solved first, next a correction of pressure is performed in order to do a correction in the mass balance, and then the mass transfer equations are solved with the new data obtained from the correction of the mass balance. Once the properties have been updated the energy equation is solved.

8. Results

8.1. Validation of the numerical model

A validation of the numerical model was conducted by reproducing the experimental performance curve reported in [24]. Fig. 6

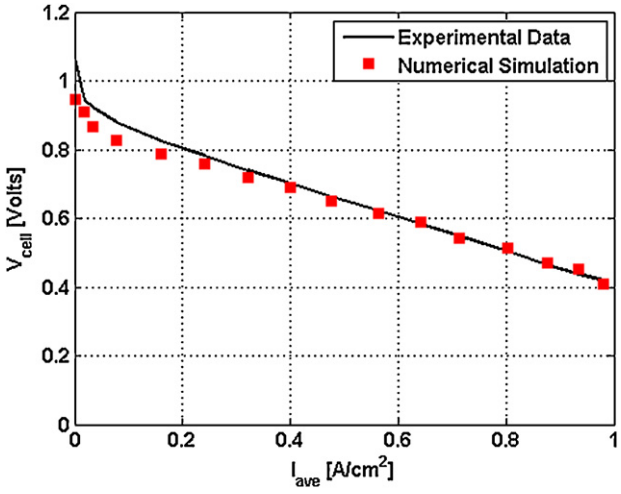

Fig. 6. Numerical validation of experimental data.

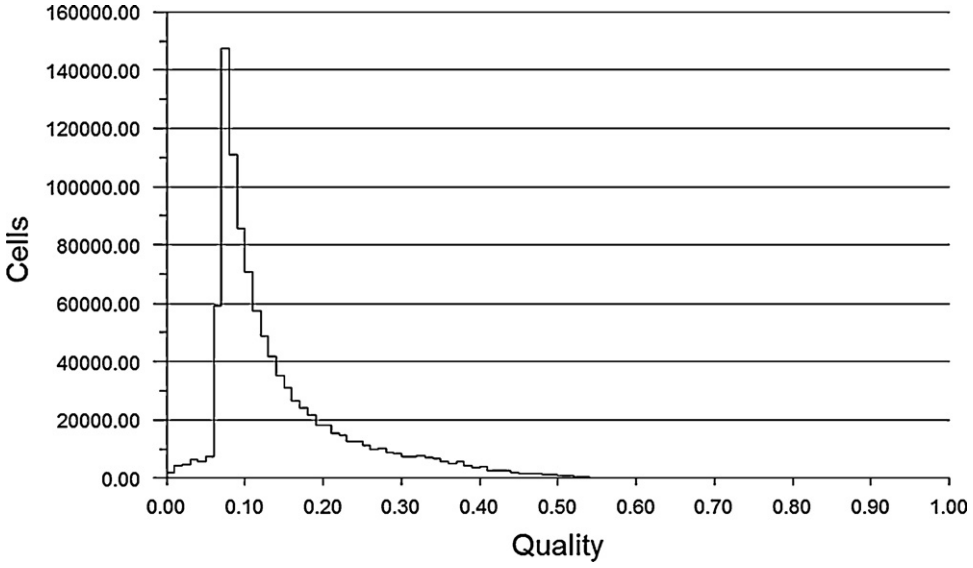

Fig. 5. Cell quality histogram. Equilateral volume deviation method.

shows the comparison between the experimental and the numerical simulation using the same operating conditions and dimensions presented by Um and Wang [24]. The comparison shows a very good agreement between numerical and experimental data. The present validation ensures that the model described so far works as a PEM fuel cell performance simulator.

8.2. Polarization and power curves

The polarization and power curves for the 6 fuel cell models analyzed are presented in Figs. 7 and 8, respectively. The polarization curves allow comparison of the overall performance of the cell under different operating conditions.

The activation losses, which occur at very low current densities (0–0.1 A cm^{-2}), were very similar for all six models, see Fig. 7, because all the cell models need almost the same amount of energy to begin the reaction.

The main difference in terms of fuel cell performance, amongst the 6 geometries proposed, is the behavior of the ohmic losses. The ohmic losses effect can be easily observed by comparing the polarization curves slope. A larger slope value means a larger ohmic losses effect. This kind of losses appears at current densities larger than 0.1 A cm^{-2}. The ohmic losses effect is most significant for the 8-channel model having a poor performance. The 4-channel and the 3-channel models have the best performance. The 2-channel and 6-channel models have a similar behavior, although not the best.

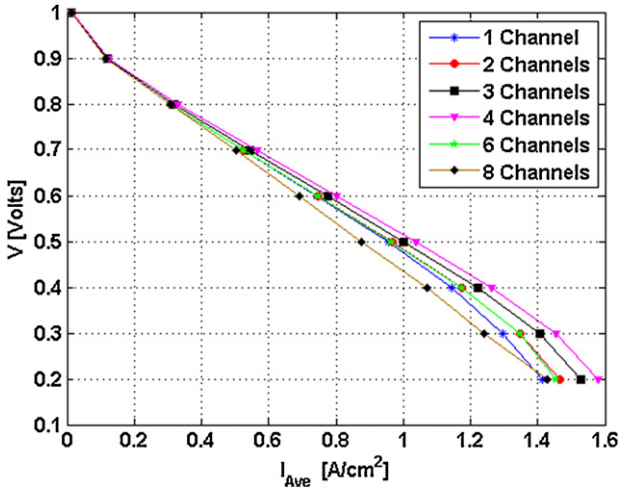

Fig. 7. Polarization curves.

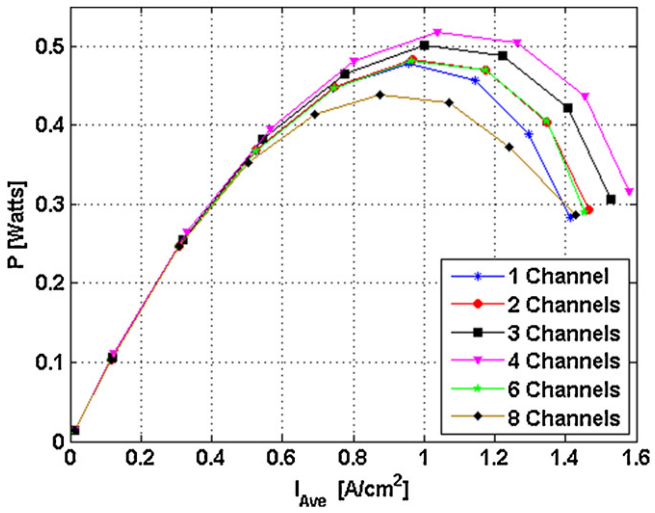

Fig. 8. Power curves.

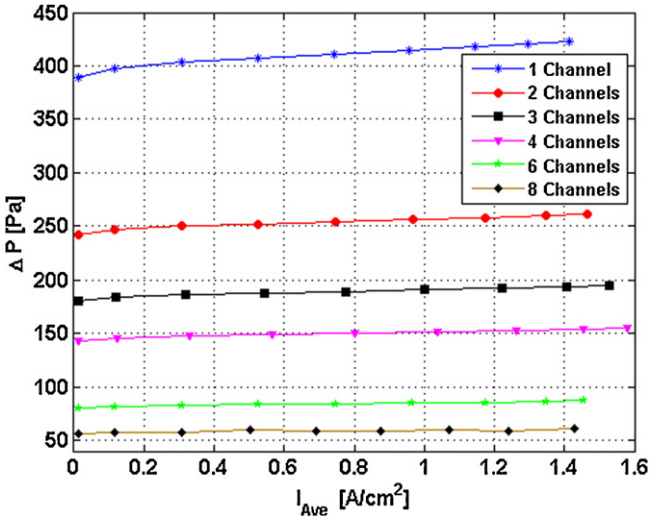

Fig. 9. Pressure drop for the cathode side.

Finally, a comparison of the power curves, see Fig. 8, supports the previous discussion. The 4-channel fuel cell is the one with the largest power developed, while the 8-channel fuel cell has the worst performance, having a maximum power difference of 15% compared to the maximum power developed for the 4-channel fuel cell.

8.3. Pressure drop

Fig. 9 shows the pressure drop on the cathode side for each of the 6 models. As shown in Fig. 9, the pressure drop increases as the number of spirals decreases. Thus, the 1-spiral fuel cell produces the largest pressure drop because the gases have to go through a larger channel compared with the channel length for the rest of the models. The cell voltage has a minimum effect on the pressure drop having a maximum difference of 10% between the maximum and minimum values.

8.4. Current density contours

For a fuel cell it is important to generate large values of electrical current, but how this is done is also important. Fig. 10 compares the current density distribution for the 6 fuel cell models. It is clear that the 4-channel fuel cell generates the electrical current in a uniform way throughout of the cell, while the 8-channel does it in an irregular way. The 8-channel fuel cell model produces a larger electrical current near the spiral center. However, at the outer zones the current produced is almost null because the reactant gases have been depleted when they reach this zone. The rest of the models have a similar distribution to that of the 4-channel model except for a lower current density value.

8.5. Distribution of gases

Although current density is a good parameter to compare cell performance, it is not the only parameter that should be taken into account. The distribution of gases through the cell is another factor used to examine the performance because it affects the current density produced, see Fig. 11. A uniform gas distribution will extend the lifetime of the membrane and will enhance the performance of the cell. The water produced by the 3-channel fuel cell accumulates

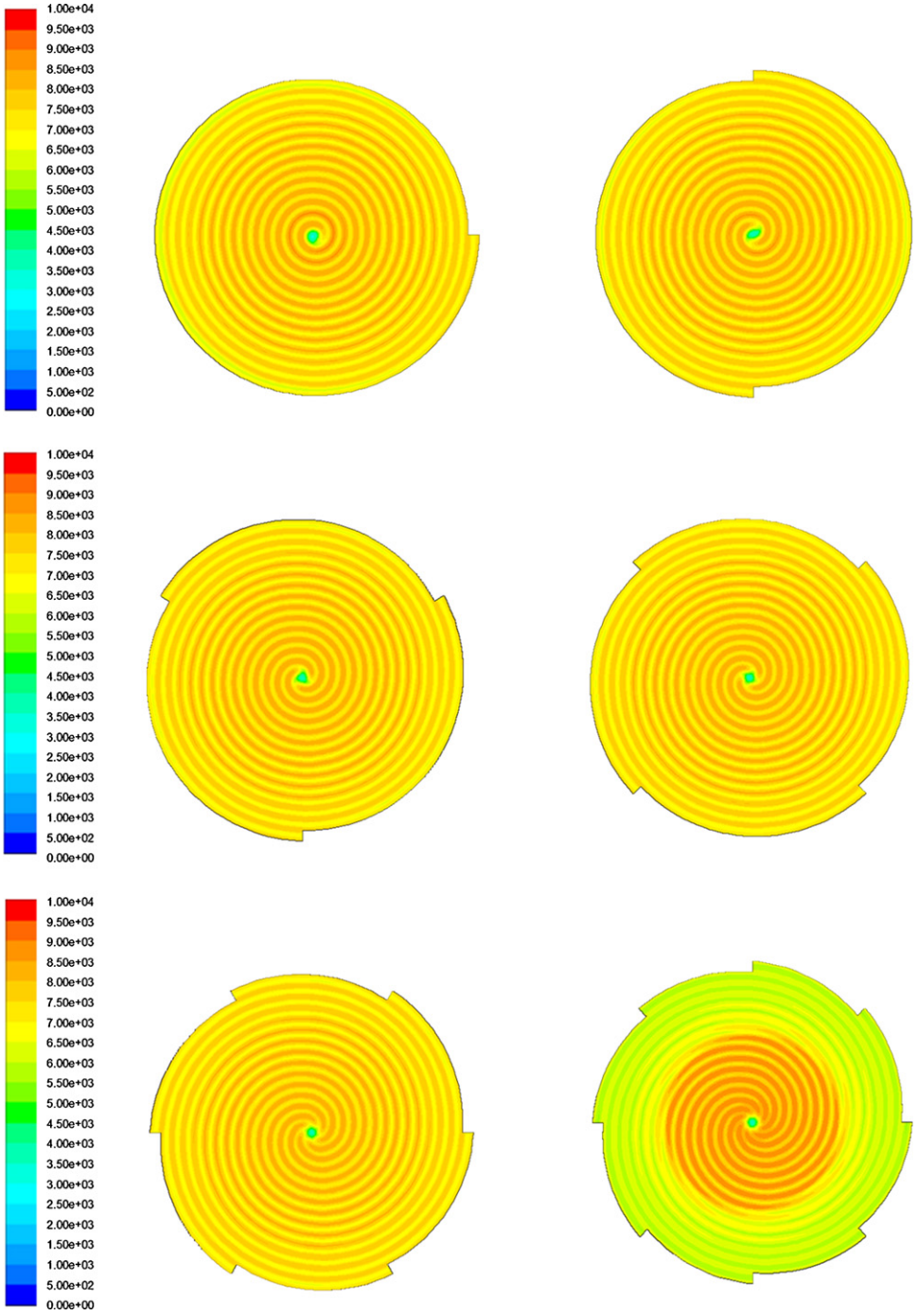

Fig. 10. Current density produced ($A\,m^{-2}$) by the six geometries at $V_{cell} = 0.6\,V$.

close to the outlets, which makes it easy to remove it. However, it also shows an irregular water production. The 8-channel fuel cell shows a more regular water production, which will help to extend the PEM lifetime.

8.6. Entropy generation by heat

Fig. 12 shows the entropy generated by each of the fuel cells geometries. Clearly, the entropy generated by heat increases as the current density increases. The heat is produced either by the Joule effect or the chemical reactions that take place in the cell. The model that generates the least amount of entropy, for a specific current density, is the 4-channel fuel cell. On the other hand, the fuel cell with 1 spiral generates the largest amount of entropy by heat. The rest of the geometries produce almost the same amount of entropy by heat.

The 4-channel fuel cell also produced the maximum entropy by heat at higher current densities. Under this condition, the number of reactions taking place inside the cell is large; this increases the heat within the cell and also the entropy produced by heat.

8.7. Entropy generation by flow (viscous effects)

The entropy generated due to the viscous effects is shown in Fig. 13. The amount of entropy produced has no significant variation compared to the current density. A comparison between heat and

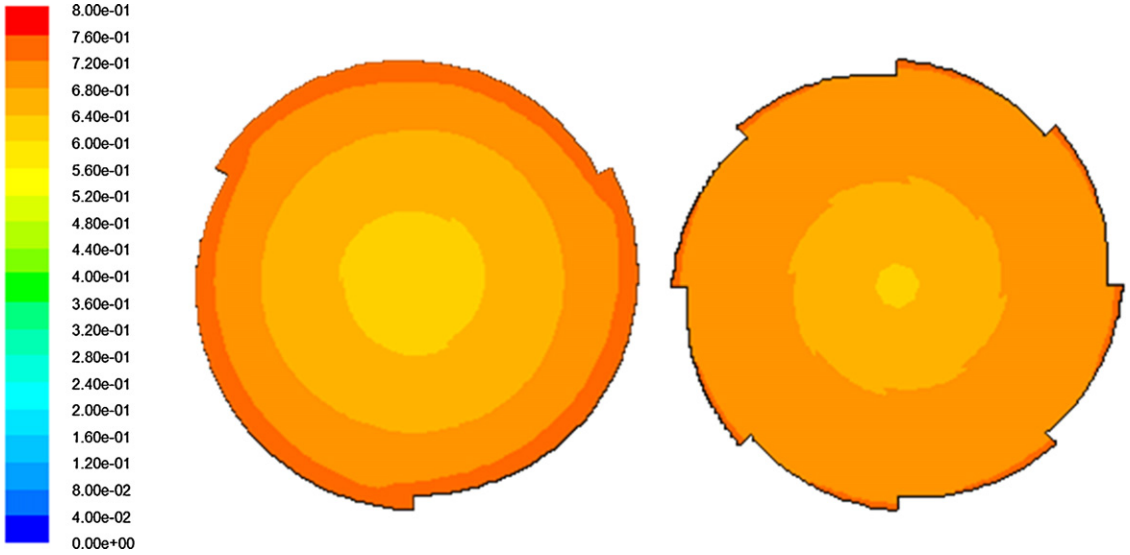

Fig. 11. Mass fraction of water at the cathode catalyst.

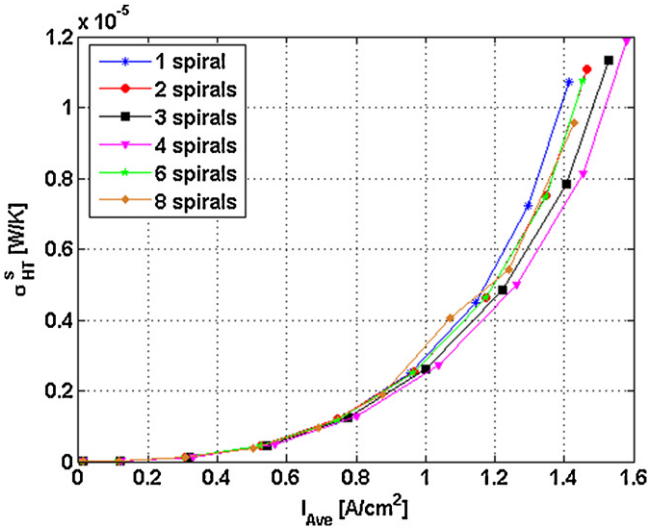

Fig. 12. Entropy generation by heat.

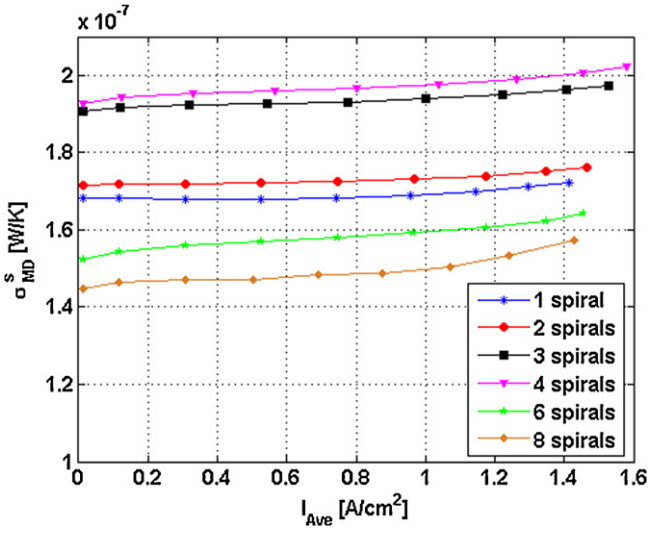

Fig. 13. Entropy generation by flow.

flow entropy produced shows that the viscous effects are almost negligible.

The 3-channel and 4-channel fuel cell produced the largest quantity of entropy due to the viscous effects. However, this parameter can be considered negligible for two reasons; first, because of its small magnitude, and second, because the two geometries are the ones that produce the best cell performance (based on the polarization and the power curves.)

8.8. Entropy generation by matter flow

Figs. 14–17 show the entropy generated by the diffusion through the cell of the hydrogen, water, nitrogen and oxygen, respectively. The entropy generation by matter flow depends mainly on the gases concentration and its capability to diffuse into the porous zone. Thus, if the quantity of entropy generated is large, it means that there is a large variation of the gas concentration from one zone to other.

The entropy generated by the hydrogen diffusion, see Fig. 14, shows that at lower current density (voltages close to the open circuit voltage) the entropy generated is larger. This is due to the fact

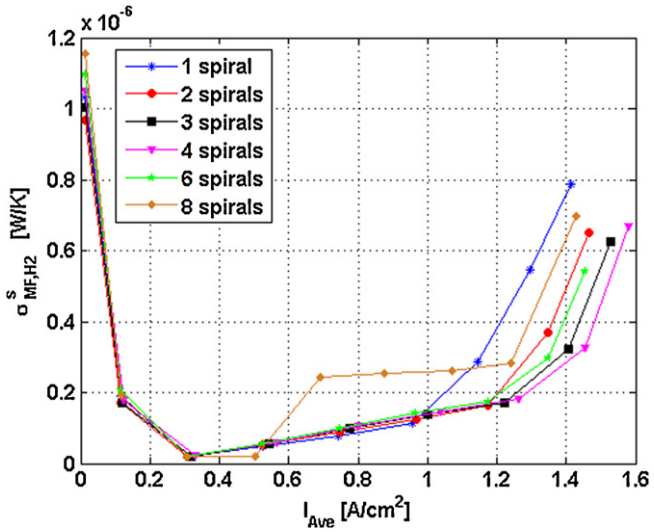

Fig. 14. Entropy generation by the H_2 diffusion.

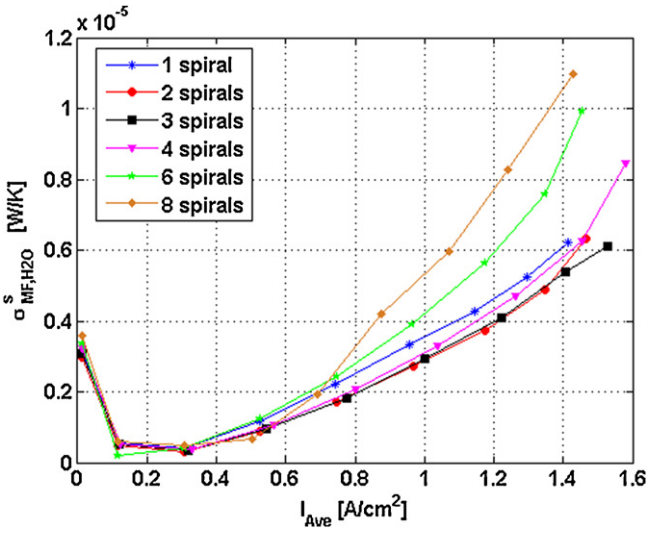

Fig. 15. Entropy generation by the H_2O diffusion.

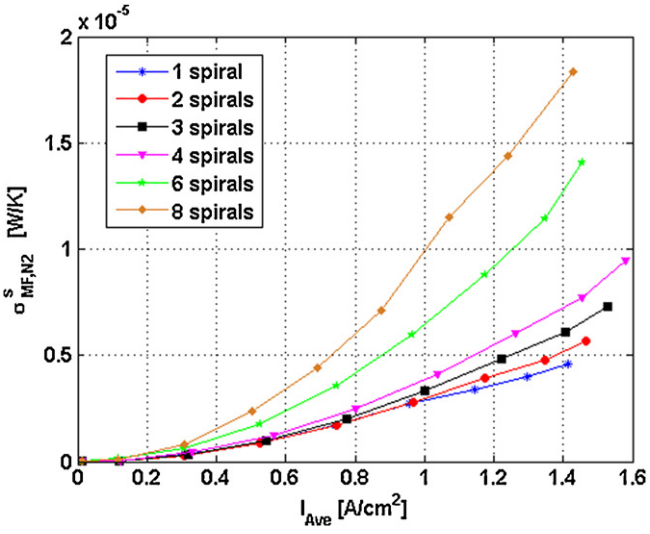

Fig. 16. Entropy generation by the N_2 diffusion.

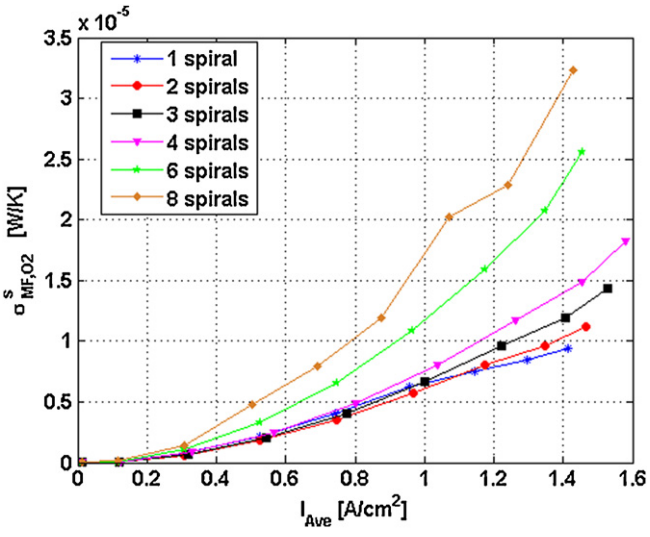

Fig. 17. Entropy generation by the O_2 diffusion.

that at lower current densities the reactions occurring in the cell are spontaneous and non-uniform. Under this condition, the hydrogen enters the cell but does not react, and its chemical potential is wasted.

However, as the current density increases, the entropy generated reaches a minimum point to increase again its value as the cell voltage is close to zero. The six geometries again produce almost the same amount of entropy, within the range of 0–1 A cm^{-2}, with the exception of the 8-channel fuel cell which shows an erratic behavior (due to the non-uniform current density production.) The main difference appears at larger current densities where the 4-channel fuel cell produces the lowest amount of entropy while the 1 channel fuel cell produces the largest.

The entropy produced by the water diffusion, see Fig. 15, has an inverse behavior than that of the hydrogen diffusion with a magnitude impact 10 times larger. The difference between the water and the hydrogen entropy production can be found by looking at how the cell works. At larger cell voltages, the water production is small because of the small current density required. As the cell voltage decreases, the current density produced increases as does the water produced. This amount of water produced should be removed from the cell through the channels. If the geometry of the channels does not help this draining effect, the cell performance diminishes. For the 8-channel and the 6-channel fuel cells, the entropy generated due to the water diffusion is large because the channels cannot remove the water surplus. On other hand, the 1, 2 and 3-channel fuel cells have no problem with this effect and they produce the lowest entropy production by water diffusion.

Nitrogen is a particular case on the fuel cells because it enters the cell joined to the oxygen as air, but it does not react. It can be considered as a cooling fluid because it takes heat from the cell before leaving it. However, its entropy contribution, see Fig. 16, is significant although the mass of nitrogen that enters the cell is the same as that observed when it exits. The nitrogen concentration variation is caused by the variation of the rest of the species. The geometries that produce the larger amount of entropy by nitrogen diffusion are the 6 and 8-channel fuel cells. The 1 and 2-channel fuel cells produce the lowest amount of entropy due to nitrogen flow.

From all the species that affect cell performance, oxygen diffusion is the one that produces the largest entropy, see Fig. 17. Once again the 6 and 8-channel fuel cells have the larger entropy production than the rest of the geometries. Contrary to the effect of the hydrogen diffusion, at large cell voltages the entropy production by oxygen diffusion is negligible because it does not have to react to accomplish the current density demanded. However, at low cell voltage, the current density produced increases considerably, producing large oxygen concentrations variations, and therefore increasing the entropy produced.

The entropy production due to matter flow is the sum of the entropy contribution of H_2, H_2O, N_2 and O_2. The total entropy produced is the sum of the contributions by means of heat, flow, and matter flow. The results are shown in Fig. 18 and they lead to the same conclusion about the best geometries (1 and 2 spirals) and the worst geometries (6 and 8 spirals) with respect to the entropy generation. Although, the performance of the 3 and 4-channel fuel cell is not bad at all, developing almost the same amount of entropy than that of the 1 and 2 channel geometries.

So far, the effects and causes of each of the processes (heat, flow and matter flow) that contribute to the net entropy generation have been compared. However, it is important to decide which one of them is the most significant.

The Bejan number is used to compare the effect of the entropy production by heat on the net entropy, see Fig. 19. Bejan numbers lower than 0.5 mean that the heat effect is not significant on the phenomena. The maximum Bejan number occurs at higher current

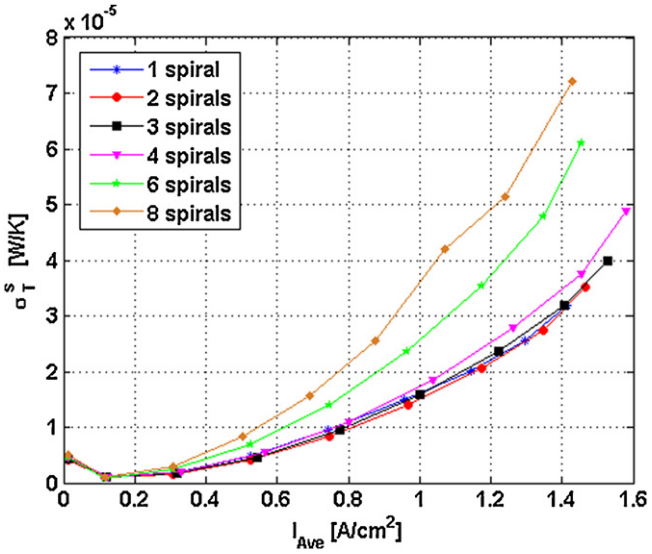

Fig. 18. Total entropy production.

densities and it decreases as long as the current density decreases. In this analysis, the maximum Bejan number is 0.33 for the 1-spiral fuel cell at a cell voltage of 0.2 Volts (I_{Ave} = 1.42 A cm^{-2}). Although, the maximum value obtained for the Bejan number represents 33% of the net entropy produced, it does not represent the main effect on the cell performance. So, instead of analyzing the cell performance using the Bejan number, it is better to analyze it with the entropy ratio, Π, proposed by Damian et al. [18], see Fig. 20.

The Π number represents the ratio of the entropy generated by matter flow on the total entropy generated. Lower Π numbers represent a more efficient fuel cell. Fig. 19 shows that the 1 and 2-channel fuel cells are the best geometries in terms of minimizing the entropy production (while the 6 and 8-channels are the worst.)

An analysis using the Bejan number will lead to conclude that the 6 and 8 channels are the best geometries because they produced the lowest entropy generation. However, the analysis using the Π number will lead to conclude that the 1 and 2-channel fuel cells are the best geometries. The way to decide which one of them is more appropriate depends on deciding what is the most important effect in the fuel cell, heat production or gas diffusion. The main function of a fuel cell is to produce current density. Current density

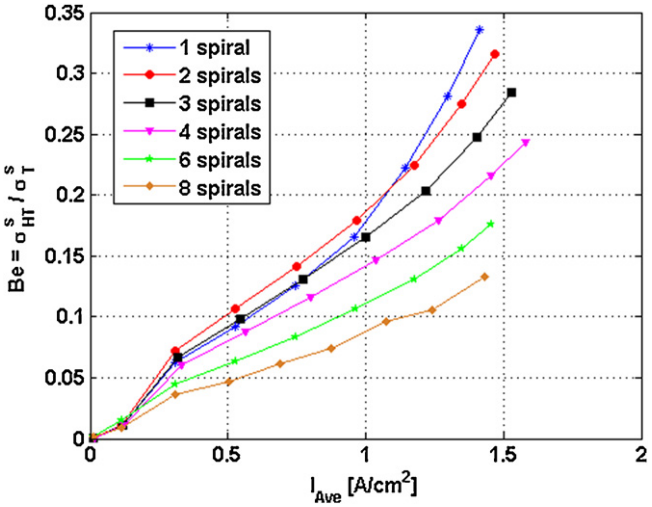

Fig. 19. Bejan number.

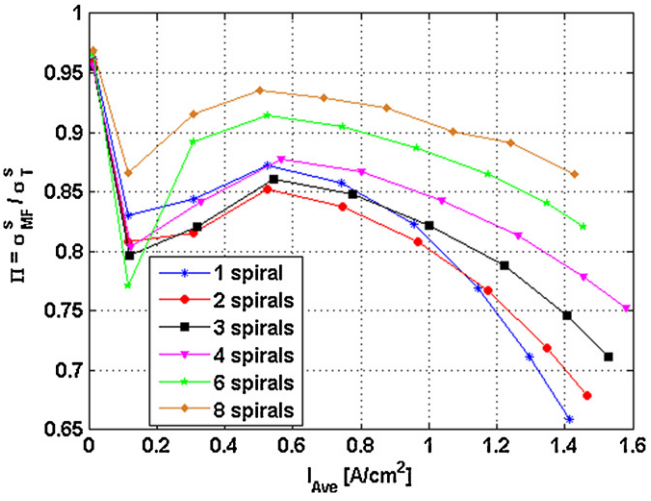

Fig. 20. Pi number.

is related to the number and distribution of the reactions occurring in the cell. The distribution of reactions depends mainly on the gases distribution; thus, the Π number is more suitable to characterize the cell performance.

9. Conclusions

The present work compares the performance of a fuel cell using six different geometries, with the Archimedes spiral as a base. The performance analysis is based on the current density produced and its distribution along the cell. Also, an entropy analysis was conducted in order to determine which of the 6 geometries proposed is the best design to minimize the entropy produced.

The model with 4 spirals is found to be the best geometry to distribute the gases. The main advantages of this model are: the larger power developed, the more uniform current density produced, a uniform management of water, and the relatively small pressure drop. The model with 8 spirals produces the worst performance of the fuel cell. The rest of the models have an average performance but, still lower than the 4-channel performance.

The present results are in complete disagreement with an earlier work [14], where the cell performance of 2 fuel cells with 1 and 2 spiral's geometry was reported. The previous result established that the 2-channel (Fermat's spiral) has a much better performance than the one with 1 spiral. The present results show a similar performance between the two models and there is not an improvement of the performance. The possible differences can be the electrochemical parameters used or the boundary conditions that are completely different. The present analysis is more acceptable due to the fact that the inlet gases conditions are calculated based on stoichiometric parameters.

The geometry that produces the least amount of entropy is the 1-channel fuel cell followed by the 2-channel fuel cell. The 3 and 4-channel fuel cell models have an average performance as compared to the other four geometries. The 6 and 8-channels models are the worst geometries, generating the maximum amount of entropy.

All things considered for the present problem lead to the following conclusions:

- The 4-channel geometry is the best option to implement as a bipolar plate. It generates the largest current density, and develops the largest power. It could be argued that it does not produce the lowest amount of entropy but its values are still reasonable good.

- The second best option for the fuel cell geometry is the 3-channel. Its performance is very similar to that of the 4-channel model but with the difference that it produces a lower current density.
- The 1-channel and 2-channel models have an average performance from all points of views, being good options if the criterion to meet is the minimum entropy generation.
- Finally, the 6-channel and the 8-channel develop the worst performance as a fuel cell. They produce the lowest current density and the largest entropy production.

Thus, the number of channels used considerably affects the cell performance, finding the optimal value between 3 or 4 channels. It is not convenient to increase the number of channels because there is not a significant improvement on the cell performance, and also the manufacturing of the flow channels becomes more complex.

Two different parameters were used to compare the cell performance based on the entropy analysis, the Bejan number and the Π number. The present results are in complete agreement with those previous results of Damian et al. [18] in that the matter flow has a more significant effect than the thermal effects. The work by Damian and the presented work enhance the use of the Π number as the best option to analyze and characterize fuel cells.

References

[1] S. Dutta, S. Shimpalee, J.W. Van Zee, W.K. Lee, Effect of humidity on PEM fuel cell performance part II—Numerical simulation, in: Proceedings of ASME IMECE, HTD 364-1, 1999, pp. 367–374.
[2] P.T. Nguyen, T. Berning, N. Djilali, Computational model of a PEM fuel cell with serpentine gas flow channels, Journal of Power Sources 130 (2004) 149–157.
[3] Pollegri A., Spaziante P.; 1980. US Patent no. 4197178.
[4] Guilin Hu, Jianren Fan, Song Chen, Three-dimensional numerical analysis of proton exchange membrane fuel cells (PEMFCs) with conventional and interdigitated flow fields, Journal of Power Sources 136 (2004) 1–9.
[5] D.L. Wool, J.S. Yi, T.V. Nguyen, Effect of the liquid water injection and interdigitated flow field on the performance of proton exchange membrane fuel cells, Electrochemical Acta 43 (1998) 3795–3809.
[6] S. Cano-Andrade, A. Hernandez-Guerrero, D. Juarez-Robles, C. Rubio-Arana, Experimental study for PEMFCs with conventional and innovative channel configurations, in: Proceedings of ECOS 2009; RS30600B, Paraná, Brazil, 2009.
[7] I. Perez-Raya, A. Hernandez-Guerrero, D. Juarez-Robles, M. Gutierrez-Rivera, J.C. Rubio-Arana, New radial-based flow configurations for PEMFCs, in: Proceedings of ASME IMECE 2009: 12202, Florida, USA, 2009.
[8] J.V.C. Vargas, J.C. Ordoñez, A. Bejan, Constructal flow structure for a PEM fuel cell, International Journal of Heat and Mass Transfer 47 (2004) 4177–4193.
[9] C.E. Damian-Ascencio, A. Hernandez-Guerrero, J.A. Escobar-Vargas, C. Rubio-Arana, F. Elizalde-Blancas, Three dimensional numerical prediction of the current density for a constructal theory-based flow field pattern, in: Proceedings of ASME IMECE 2007; 42449, Seattle, USA, 2007.
[10] A. Chapman, I. Mellor, Development of biomimetic flow field plates for PEM fuel cells, in: Eighth Grove Fuel Cell Symposium, London, UK, 2003.
[11] S. Senn, D. Poulikakos, Tree network channels as fluid distributors constructing double staircase polymer electrolyte fuel cells, Journal of Applied Physics 96 (2004) 842–852.
[12] B. Ramos-Alvarado, A. Hernandez-Guerrero, D. Juarez-Robles, J.C. Rubio-Arana, Analysis of flow distribution in a symmetric bipolar plate for PEMFC, in: Proceedings of ECOS 2009, Paraná, Brazil, 2009.
[13] J.A. Escobar-Vargas, A. Hernandez-Guerrero, A. Alatorre Ordaz, C.E. Damian-Ascencio, F. Elizalde-Blancas, Performance of a non-conventional flow field in a PEMFC, in: Proceedings of ECOS 2007, 2007, pp. 1083–1091.
[14] D. Juarez-Robles, A. Hernandez-Guerrero, C.E. Damian-Ascencio, J.C. Rubio-Arana, Three dimensional analysis of a PEM fuel cell with the shape of a Fermat spiral for the flow channel configuration, in: Proceedings of IMECE 2008; 68101, Chicago, USA, 2008.
[15] K. Tüber, A. Oedegaard, M. Hermann, C. Hebling, Investigation of fractal flowfields in portable proton exchange membrane and direct methanol fuel cells, Journal of Power Sources 131 (2004) 175–181.
[16] A. Bejan, Second-law analysis in heat transfer and thermal design, Advanced Heat Transfer 15 (1982) 1–58.
[17] A. Bejan, Entropy Generation Minimization, CRC Press, Boca Raton, New York, 1996.
[18] C.E. Damian-Ascencio, A. Hernandez-Guerrero, F. Ascencio-Cendejas, D. Juarez-Robles, Entropy generation analysis for a PEM fuel-cell with a biomimetic flow field, in: Proceedings of ASME IMECE 2009, 12057, Florida, USA, 2009.
[19] J.H. Nam, M. Karviany, Effective diffusivity and water-saturation distribution in single and two-layer PEMFC diffusion medium, International Journal of Heat Mass Transfer 46 (24) (2003) 4595–4611.
[20] T. Nguyen, R. White, A water and heat management model for proton-exchange-membrane fuel cells, Journal of Electrochemistry Society 140 (1993) 2178–2186.
[21] T.E. Springer, A. Zawodzinski, S. Gottesfeld, Polymer electrolyte fuel cell model, Journal of Electrochemistry Society 138 (1991) 2334–2341.
[22] A. Parthasarathy, S. Srinivasan, J. Appleby, Journal of Electrochemistry Society 139 (1932) 2530.
[23] D. Jou, J. Casas-Vazquez, G. Lebon, Extended irreversible thermodynamics, Edit. Springer, Germany, 1996.
[24] S.M. Sukkee Um, C.Y. Wang, Three-dimensional analysis of transport and electrochemical reactions in polymer electrolyte fuel cells, Journal of Power Sources 125 (2004) 40–51.
[25] D. Senn, Poulikakos, Polymer electrolyte fuel cells with porous materials as fluid distributors and comparisons with traditional channeled systems, Journal of Heat Transfer 123 (3) (2004).